

5

1
2

The Monojet Analysis

3 As has been described in Chapter 2, there are many searches for dark matter both at particle accelerators
4 and elsewhere. At the LHC, one very promising channel is the so-called monojet search, where the
5 detection of dark matter is done by looking for missing energy in association with one or more jets. The
6 dark matter particles are expected to pass through the detector without leaving any signal since they are
7 neutral and only interact very weakly. They can however be detected indirectly as missing energy when
8 they recoil off one or more jets coming from initial state radiation.

9 First, the used physics objects are described in Section 5.1. Next, the selection of the events using the
10 trigger is described in Section 5.2, and the subsequent event selection performed with fully reconstructed
11 events is detailed in Section 5.3. The estimation of the background and the included systematic uncer-
12 tainties are described Section 5.4 and 5.5, respectively. In Section 5.6, the obtained results are shown.
13 The improvements achieved by going from the analysis strategy used in 2015 to the 2016 version are
14 detailed in Section 5.7. Finally, the results are interpreted in terms of the considered dark matter models
15 in Section 5.8.

16 **5.1 Physics object reconstruction**

17 While jets are evidently important objects in this analysis, other physics objects are used as well. Leptons
18 and photons are for example vetoed in order to reject backgrounds, and are used to define the many
19 control regions used for the background prediction.

20 **5.1.1 Jets**

21 The method described in Section 4.3.7 is used to reconstruct the used PF jets, and the jet energy cor-
22 rections are applied as well. Furthermore, the jets are required to have $p_T > 30 \text{ GeV}$, and to pass the
23 loose jet identification and pileup jet identification described in Section 4.3.7. Additionally a jet cleaning
24 is applied by requiring a jet charged hadron energy fraction CHF > 0.1 and a jet neutral hadron energy
25 fraction NHF < 0.8 . The jets are also tagged as b-jets using the Combined Secondary Vertex algorithm
26 described in Section 4.3.8, with the loose working point.

27 **5.1.2 Leptons**

28 Electrons are considered for the lepton veto if they pass the loose electron selection, described in Sec-
29 tion 4.3.3, and have $p_T > 10 \text{ GeV}$ and $|\eta| < 2.5$. Similarly, muons are required to pass the loose muon
30 identification described in Section 4.3.5 and to have $p_T > 10 \text{ GeV}$ and $|\eta| < 2.4$. In the case of tau lep-
31 tons, they are required to have $p_T > 15 \text{ GeV}$ and $|\eta| < 2.3$. They should also pass the tau identification

1 criteria, which require a jet with an identified subset of particles with a mass consistent with the decay
 2 products of a hadronic tau and which are isolated with a pileup corrected isolation cut requiring less than
 3 5 GeV of energy deposits within a radial cone of $\Delta R < 0.3$.

4 The selection of electrons and muons for the dielectron, dimuon, single electron, and single muon
 5 control regions is however stricter. In this case, at least one electron or muon is required to pass the tight
 6 identification.

7 5.1.3 Photons

8 Photons are required to have $p_T > 15$ GeV, $|\eta| < 2.5$, and to pass the loose identification criteria
 9 described in Section 4.3.3, in order to be considered for the photon veto. For the photon + jets control
 10 region, photons are required to pass the tight photon identification in order to be considered.

11 5.2 Trigger selection

12 In order to select events that have the Monojet signature displayed in Figure 5.1, the trigger requires either
 13 $E_T^{miss} > 90$ GeV, where E_T^{miss} is the magnitude of the negative vectorial sum of the p_T of all particles at
 14 trigger level, or $H_T^{miss} > 90$ GeV, where H_T^{miss} is calculated as the magnitude of the negative vectorial
 15 sum of the momenta of all jets with $p_T > 20$ GeV. In order to avoid collecting noise events, tight
 16 requirements are placed on the jets used in the H_T^{miss} computation. Jet energy correction are already
 17 applied at the HLT-level and the jet NHF is required to be smaller than 0.9. Muons are not taken into
 18 account to compute E_T^{miss} and H_T^{miss} , so that the same trigger can be used to select the events for the
 19 muon control regions used for the background prediction.

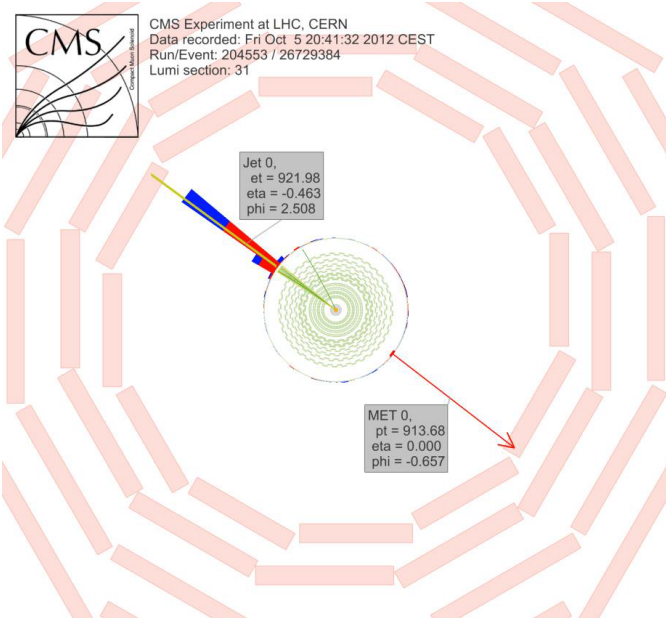


Figure 5.1: Event display showing the monojet final state.

20 This trigger is evaluated using events passing the single electron trigger with a threshold of $p_T >$
 21 23 GeV, and applying an extra offline selection requiring an electron with $p_T > 40$ GeV passing the
 22 tight identification and a jet with $p_T > 100$ GeV and $|\eta| < 2.5$. The trigger efficiency is computed by
 23 determining the fraction of events passing the signal triggers, as a function of the recoil. The efficiency is
 24 above 98% for events passing the analysis selection described below, as shown in Figure 5.2.

25 For the electron control regions, a single electron trigger was used with a threshold at $p_T > 27$ GeV.
 26 The efficiency of this trigger is determined as a function of p_T and η . This is done by “tagging” one
 27 electron and “probing” a second one, while requiring the invariant mass of this pair to correspond to the

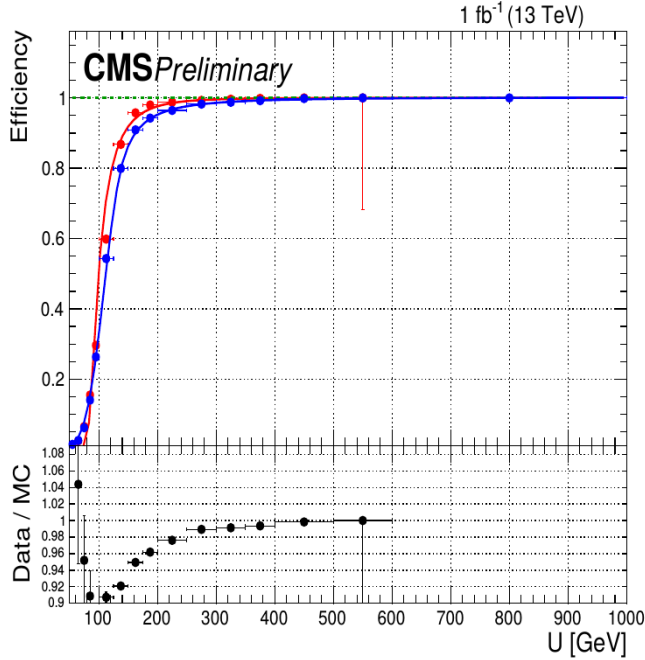


Figure 5.2: The efficiency of the used signal triggers as a function of the recoil, in MC (red) and data (blue).

¹ Z boson mass. This tag-and-probe method ensures that backgrounds are removed and allows to measure
² the efficiency by simply taking the fraction of probes that passes the single electron trigger. The obtained
³ trigger turn on curves as a function of the electron transverse momentum are shown in Figure 5.3 for the
⁴ two η bins.

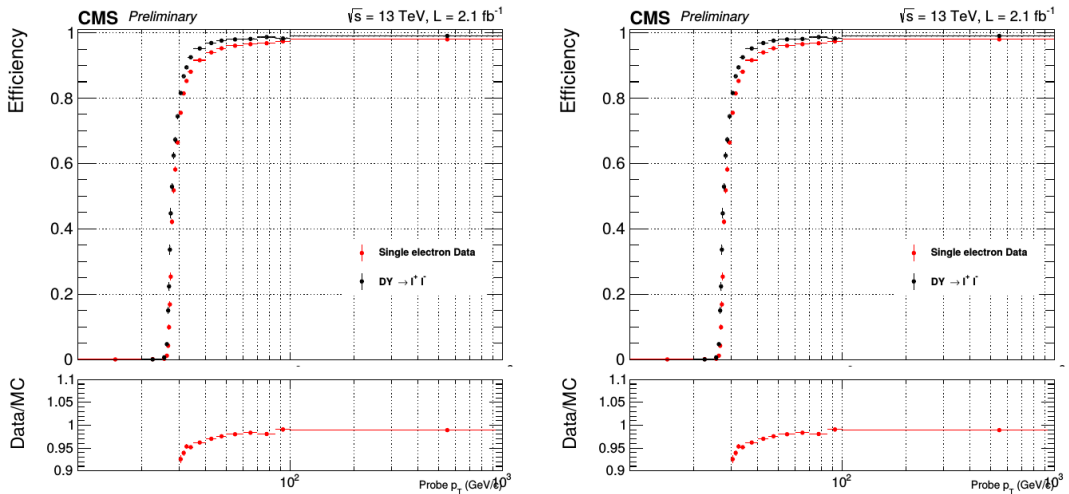


Figure 5.3: The efficiency of the single electron trigger in data (red) and MC (black) for $|\eta| < 1.4442$ (left) and $1.566 < |\eta| < 2.5$ (right).

⁵ Finally, the events in the photon control region are selected with a single photon trigger requiring an
⁶ isolated photon with $p_T > 175 \text{ GeV}$. The performance of this trigger is measured using data selected
⁷ with a looser single photon trigger.

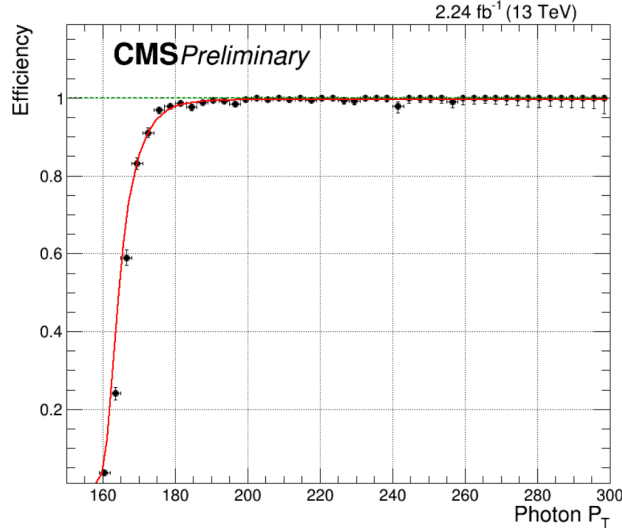


Figure 5.4: The efficiency of the single photon trigger measured in data.

5.3 Event selection

Once the events have been fully reconstructed and the jets in the event have been corrected as described in Section 4.3.7, an event selection is applied by requiring the missing transverse energy E_T^{miss} defined in Section 4.3.10 to be larger than 200 GeV in order to be consistent with the trigger turn-on. Additionally, the leading jet is required to have $p_T > 100$ GeV, and $|\eta| < 2.5$. A cut on the difference in azimuthal angle between the E_T^{miss} and the first four leading jets of $\Delta\phi(jet, E_T^{miss}) > 0.5$ is also applied to suppress the QCD background from mismeasurements of jet momentum or detector noise. The events are further cleaned by applying quality filters to remove events with badly reconstructed missing transverse energy. Finally, events containing a lepton, a photon, or a b-jet are vetoed as well. Figure 5.5 shows the E_T^{miss} distribution for the data and background prediction, after applying the described selection.

The leptons are vetoed to suppress the electroweak backgrounds, such as $W(l\nu) + \text{jets}$ and semileptonic diboson decays, while the photon veto is added to suppress the $Z(\nu\nu) + \text{photon} + \text{jets}$ and $W(l\nu) + \text{photon} + \text{jets}$ background processes, and to ensure there is no overlap with a similar dark matter search which investigates the final state consisting of missing energy and a photon. This rejects less than 1% of the signal. Finally, the b-jet veto reduces the top background by a factor 3 and only reduces the signal by 5 to 10%, depending on the type and mass of the mediator. No additional veto on the number of jets is applied.

5.4 Background estimation

The dominant background comes from $Z + \text{jet}$ events where the Z boson decays to two neutrinos. This produces the same signature of jets with missing energy as the signal, and results in an irreducible background. The second largest background consists of $W + \text{jets}$ events with a leptonically decaying W boson. This background is already suppressed by the lepton veto, but a fraction of these events remain when the lepton is either not identified or outside of the detector acceptance. The remaining background events come from top quark decays, which are suppressed by the b-jet veto, semileptonic diboson (WW , WZ , and ZZ) decays, and QCD multijet events. The two main background contributions are estimated from five control regions in data consisting of dimuon, dielectron, single muon, single electron, and photon + jets events. The E_T^{miss} in these control regions is redefined in order to imitate the E_T^{miss} shape in the signal region. This hadronic recoil U is obtained by removing the leptons or the photon from the E_T^{miss} computation. The contributions from top quark decays and semileptonic diboson decays are estimated using simulated samples, while the QCD multijet background is estimated using a data-driven approach.

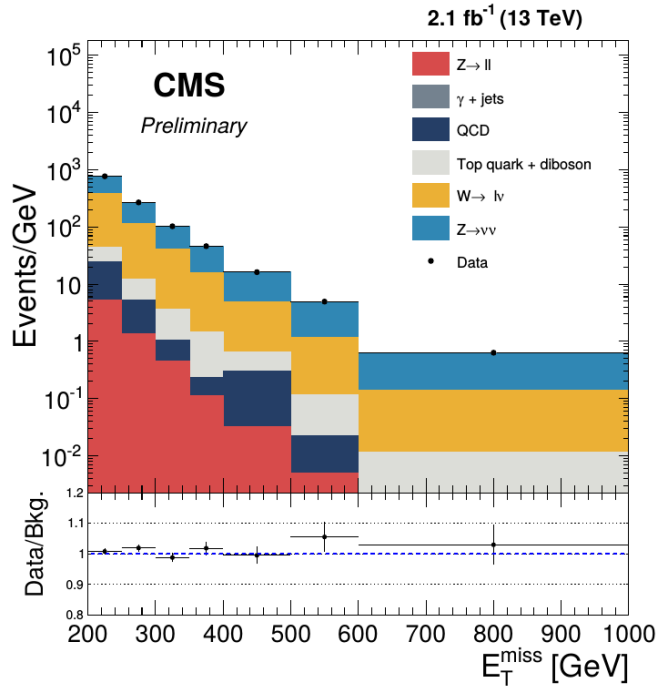


Figure 5.5: The missing transverse energy distribution after applying the described event selection, for the data and the predicted backgrounds.

5.4.1 The Z and W background estimation

The yield of $Z(\nu\nu)$ and $W(l\nu) + \text{jets}$ events in the signal region is estimated from five control regions by using the ratio between data and MC in the control region, per bin of the recoil distribution. For the prediction using $Z \rightarrow \mu\mu$ events in the dimuon control region for example, the predicted yield of $Z \rightarrow \nu\nu$ events is given by

$$N_{Z(\nu\nu)} = \frac{N_{Z(\mu\mu)}^{\text{data}}}{N_{Z(\mu\mu)}^{\text{MC}}} N_{Z(\nu\nu)}^{\text{MC}} \quad (5.1)$$

$$= \frac{N_{\mu\mu}^{\text{data}} - N_{\text{Bkgd}}}{N_{Z(\mu\mu)}^{\text{MC}}} N_{Z(\nu\nu)}^{\text{MC}} \quad (5.2)$$

$$= \frac{N_{\mu\mu}^{\text{data}} - N_{\text{Bkgd}}}{N_{Z(\mu\mu)}^{\text{MC}}} R_{Z(\mu\mu) \rightarrow Z(\nu\nu)} N_{Z(\mu\mu)}^{\text{MC}} \quad (5.3)$$

- 2 The transfer factors, denoted by R , are derived from simulation and take into account the impact of lepton
 3 acceptance and efficiency, as well as the additional E_T^{miss} requirement for the single electron control
 4 region. They also include the difference in branching ratio and the relation between the differential cross
 5 sections of the photon, W , and Z boson production as a function of the boson p_T . The transfer factors
 6 are computed as a function of the recoil, and are shown for the five different control regions in Figure 5.6.
 7 Furthermore, the Z/W ratio shown in the bottom right plot of Figure 5.6 provides an additional constraint
 8 since the single lepton control regions are also used to estimate the $Z(\nu\nu) + \text{jets}$ background.

9 The simulated samples used for the background estimation are generated at leading order (LO) using
 10 the MADGRAPH generator, and corrected to next-to-leading order (NLO). These corrections introduce an
 11 additional systematic uncertainty, but are crucial in order correctly represent the data, since the simulation
 12 is approximately 40% higher than the data when using only LO calculations. The NLO QCD k-factors
 13 are derived from samples generated at NLO with MADGRAPH5_aMC@NLO, while the electroweak k-
 14 factors are obtained from theoretical calculations [130–133]. The differential cross section as a function
 15 of the boson p_T is shown in Figure 5.7 for photon, W , and Z production, and the obtained k-factors

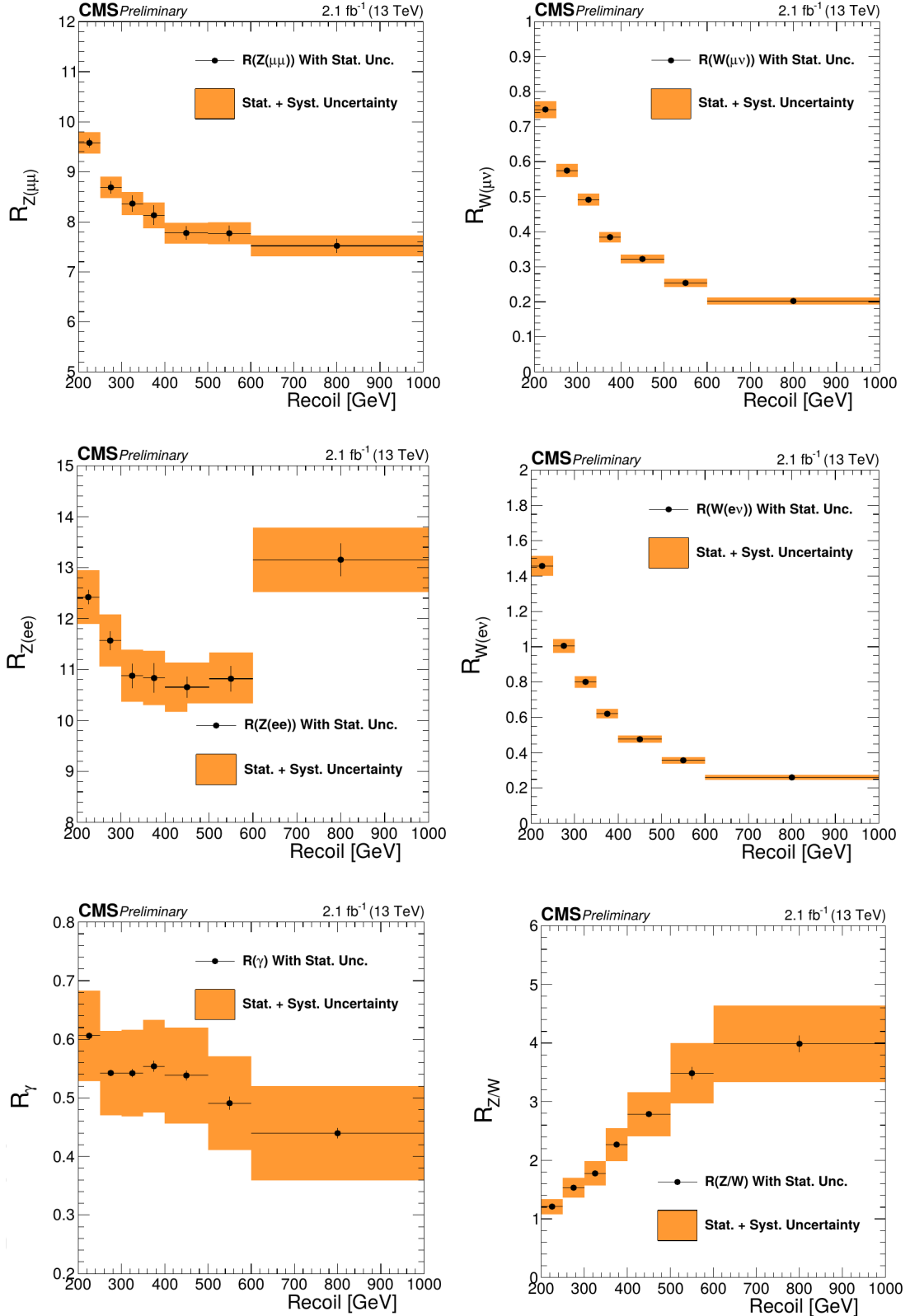


Figure 5.6: Transfer factors for the dimuon (top left), single muon (top right), dielectron (middle left), single electron (middle right), and photon + jets (bottom left) control regions. The ratio of the Z and W transfer factors is shown in the bottom right plot.

1 are displayed in the ratio plots. More details on the different control regions are given in the following
2 description.

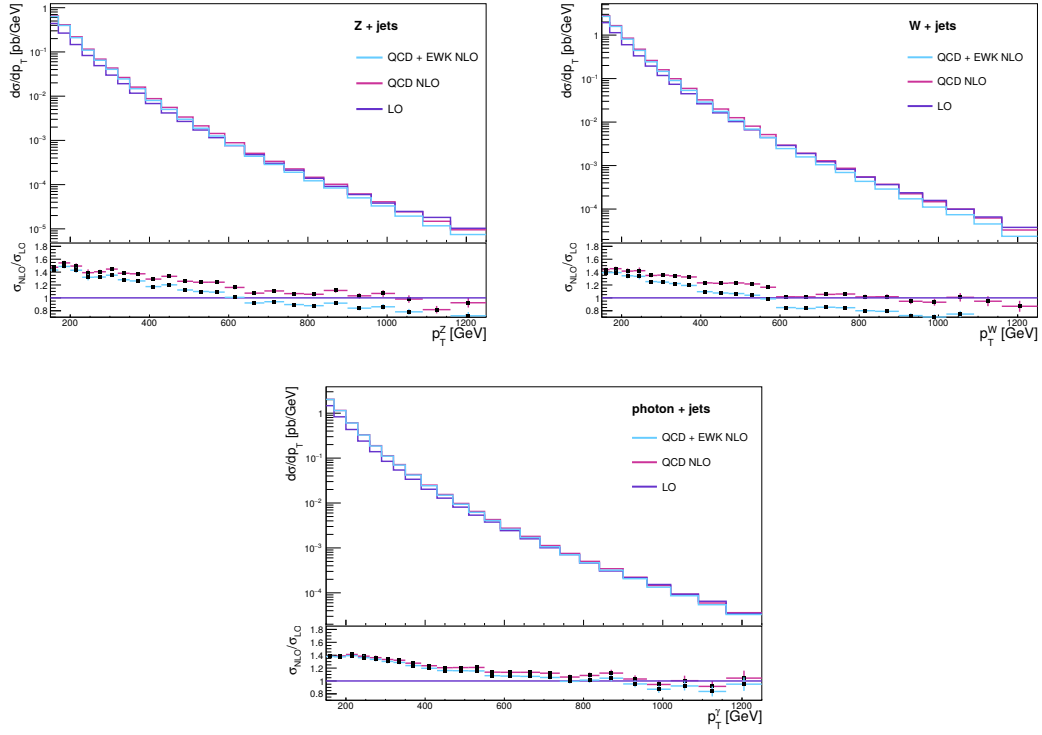


Figure 5.7: The differential cross section as a function of the boson p_T for photon, W , and Z production, using boson p_T -binned NLO samples. The resulting k-factors are shown in the ratio plots.

Dimuon control region

The traditional control region for the Z boson background is the dimuon control region. This region is dominated by $Z \rightarrow \mu\mu$ events, which are very similar to the $Z(\nu\nu) + \text{jets}$ background events, the only difference being the decay mode. The production mode and kinematics in the control region are very similar, as well as the acceptance. However, the branching ratio of the Z boson into two muons is 6 times smaller than the branching ratio to two neutrinos. As a result, the dimuon control region contains about 10 times less Z boson events than the signal region. In order to improve this statistical limitation, other control regions have been added as well.

In the dimuon control region the events are selected using the monojet triggers and applying the same requirements as described in Section 5.3 for the signal region, using the recoil instead of the missing transverse energy, except for the muon veto. Additionally, exactly two muons with opposite charge and with $p_T > 10$ GeV should be identified using the loose identification. The leading muon should have a transverse momentum large than 20 GeV, and at least one muon should pass the tight selection requirements. Finally, the dimuon mass should be between 60 and 120 GeV, corresponding to the Z boson mass.

Single muon control region

In order to model the second largest background, coming from $W(l\nu) + \text{jets}$ events, a single muon control region is typically used. This control region is in addition also used to constrain the $Z(\nu\nu) + \text{jets}$ background. The events in the single muon control region are required to pass the monojet triggers and event selection replacing the E_T^{miss} by the recoil obtained by removing the muon, except for the muon veto. One muon should then pass the tight selection requirements and have $p_T > 20$ GeV.

1 **Dielectron control region**

2 The dielectron control region is used to constrain the $Z \rightarrow \nu\nu$ background. The events are selected
 3 by the single electron triggers. Similarly to the dimuon control region, the events are required to
 4 pass the monojet selection, except for the electron veto. Instead, exactly two electrons with $p_T >$
 5 10 GeV are required to pass the loose identification described in Section 4.3.3. In addition, at least
 6 one electron should pass the tight selection requirements, and the leading electron is required to
 7 have $p_T > 40$ GeV in order to be consistent with the single electron trigger. Finally, the dielectron
 8 mass should be between 60 and 120 GeV, in order to be consistent with a Z boson decay. The
 9 jump that can be observed in the last bin of the resulting transfer factor in the middle left plot of
 10 Figure 5.6 is due to the isolation requirement of the single electron trigger. This was verified by
 11 removing the trigger selection in MC, yielding a flat transfer factor.

12 **Single electron control region**

13 The single electron control region is used to constrain the $W(l\nu) + \text{jets}$ background. In the single
 14 electron control region, the events are required to have one electron with $p_T > 40$ GeV passing
 15 the tight selection requirements, analogously to the single muon control region. In this region, a
 16 large amount of QCD background is however present. In order to reject most of those events, an
 17 additional cut on the E_T^{miss} , which includes the single electron, is added at 50 GeV. This reduces
 18 the QCD background by an order of magnitude.

19 **Photon + jets control region**

20 Due to its large yield, photon + jets control region provides the dominant constraint on the high- p_T
 21 part of the $Z(\nu\nu) + \text{jets}$ background. The selection of these events is done using the single photon
 22 triggers and applying the monojet selection, except for the photon veto. One photon is then required
 23 to pass the tight identification and to have $p_T > 175$ GeV. Additionally, it should be reconstructed
 24 inside the ECAL barrel ($|\eta| < 1.4442$) in order to achieve a high purity of 95%. Events with
 25 more than one photon passing the loose identification requirements described in Section 4.3.3 are
 26 rejected.

27 **5.4.2 The QCD background estimation**

28 While QCD multijet background events are generally well balanced in the transverse plane, missing trans-
 29 verse energy can arise in the event due to jet energy mismeasurements, punch-through, uninstrumented or
 30 defective regions in the detector, hot spots, or neutrinos from decays of heavy-flavour mesons. Although
 31 these effects are very rare, the QCD production cross section is gigantic and some events can be selected
 32 at high missing transverse energy. The event selection detailed in Section 5.3 was designed to suppress
 33 contributions from the QCD multijet background, reducing it to the percent level. However, this back-
 34 ground is not well reproduced in the simulation, and thus requires a background estimation using a data
 35 control region.

36 The yield is predicted by combining two different approaches, namely the “rebalance and smear”
 37 technique and the $\Delta\phi$ extrapolation method. The rebalance and smear technique uses a kinematic fit with
 38 the constraint that no missing transverse energy is present in the event. The event is then rebalanced by
 39 varying each jet and the remaining hadronic recoil within their computed uncertainties. The resulting
 40 jets are then smeared with the measured jet resolution, and the prediction for the QCD E_T^{miss} distribu-
 41 tion is obtained. For the $\Delta\phi$ extrapolation method, the QCD background is estimated in the region with
 42 an inverted $\Delta\phi$ selection cut, $\min \Delta\phi(\text{jet}, E_T^{\text{miss}}) < 0.5$, and then translated to the signal region us-
 43 ing transfer factors derived from simulated events. The obtained estimation using this method yields a
 44 contribution that is a factor 2 larger than the prediction from simulation, which agrees well with the the
 45 rebalance and smear technique, as can be seen in Figure 5.8.

46 **5.4.3 Simulation-based background estimation**

47 Contributions are also expected from diboson production, from t quark decays, both from $t\bar{t}$ and single
 48 top production, and from $Z(l\ell) + \text{jets}$ events where the leptons are not detected. These backgrounds are

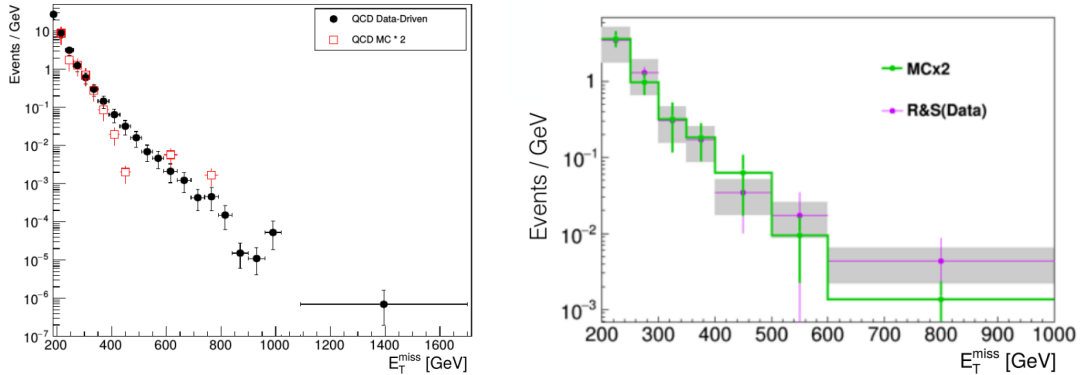


Figure 5.8: Predicted E_T^{miss} distribution of the QCD multijet background obtained using the $\Delta\phi$ extrapolation method (left) and the rebalance and smear technique (right), using data (black) and MC simulations (red). The simulation is scaled by a factor 2.

1 estimated from MC simulations.

2 Top quarks typically decay into a W boson and a b quark. When the W boson decays leptonically,
3 a neutrino is produced, generating genuine missing transverse energy. If the event is not removed by the
4 b -jet veto and the lepton is not identified, this type of events contributes to the background in the signal
5 region. However, due to the small production cross section and the applied event selection, only a small
6 fraction of these events are selected. In order to estimate the contribution of this background, a $t\bar{t}$ sample
7 has been produced at LO with MADGRAPH, and single top events were generated with PowHEG at NLO.

8 When one of the weak bosons produced in diboson events decays leptonically, generating one or more
9 neutrinos, and the other one decays hadronically, jets and missing transverse energy are produced. The
10 samples used to estimate this background have been produced using PYTHIA.

11 Finally, when the leptons in $Z(l\bar{l}) + \text{jets}$ events are lost or out of the detector acceptance, these events
12 can mimic the monojet signature as well. MC samples have been generated at LO using MADGRAPH in
13 several bins of H_T in order to estimate the contribution from this sub-dominant background.

14 5.5 Systematic uncertainties

15 For the main backgrounds, multiple systematic uncertainties on the transfer factors are taken into account.
16 Experimental uncertainties are added for the muon efficiency, the electron efficiency, the lepton veto, the
17 photon efficiency, and the photon purity in the photon + jets sample.

18 Uncertainties are also added from theory, to take into account variations of the factorization and renor-
19 malization scales, PDF uncertainties, and the NLO electroweak corrections. The former 3 uncertainties
20 are shown in Figure 5.9 for the $Z + \text{jets}$, $W + \text{jets}$, and photon + jets samples. The uncertainties are then
21 propagated to the transfer factors, and are displayed in Figure 5.10. To evaluate the PDF uncertainty, the
22 samples are reweighted with event-by-event scale factors representing the shift in the kinematic distribu-
23 tions from variations in the PDF. The transfer factors are then produced for each variation, and the RMS
24 of the variation is taken as PDF uncertainty. Similarly, the renormalization and factorization scales are
25 varied up and down by a factor 2, and the uncertainties are derived from the resulting transfer factors. For
26 the electroweak corrections, the full correction is taken as an uncertainty.

27 For the remaining sub-dominant backgrounds, systematic uncertainties are included to take into ac-
28 count the uncertainties from the jet energy scale and the jet energy resolution of the jets. Additionally,
29 systematic uncertainties of 10%, 29%, and 50% are added to account for the uncertainty on the pro-
30 duction cross section of the top, diboson, and QCD processes, respectively. For the top backgrounds,
31 a systematic uncertainty of 4% is included as well, due to the uncertainty on the b -tagging applied for
32 the b -jet veto. Finally, a systematic uncertainty of 5.5% is added for all backgrounds derived from MC
33 simulations, to take into account the luminosity measurement.

34 Lastly, for the signal models, systematic uncertainties are included for the luminosity and to take

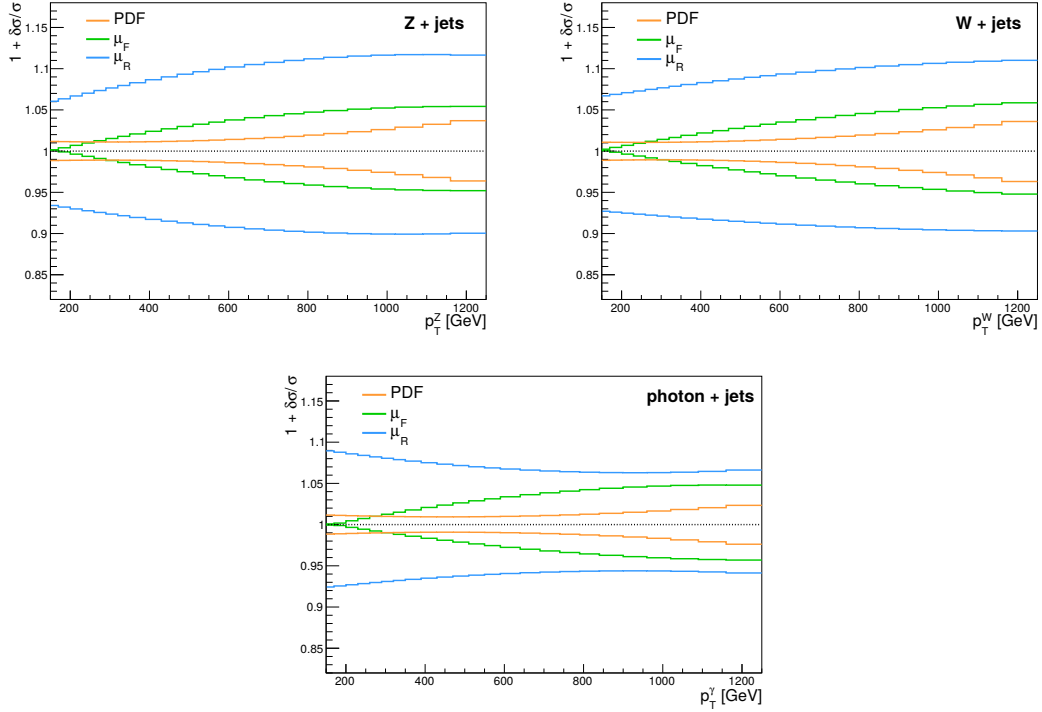


Figure 5.9: The PDF, renormalization, and factorization scale uncertainties for the $Z + \text{jets}$ (top left), $W + \text{jets}$ (top right), and photon + jets (bottom) samples. The uncertainties from the renormalization and factorization scales are obtained by separately varying them up and down by a factor 2.

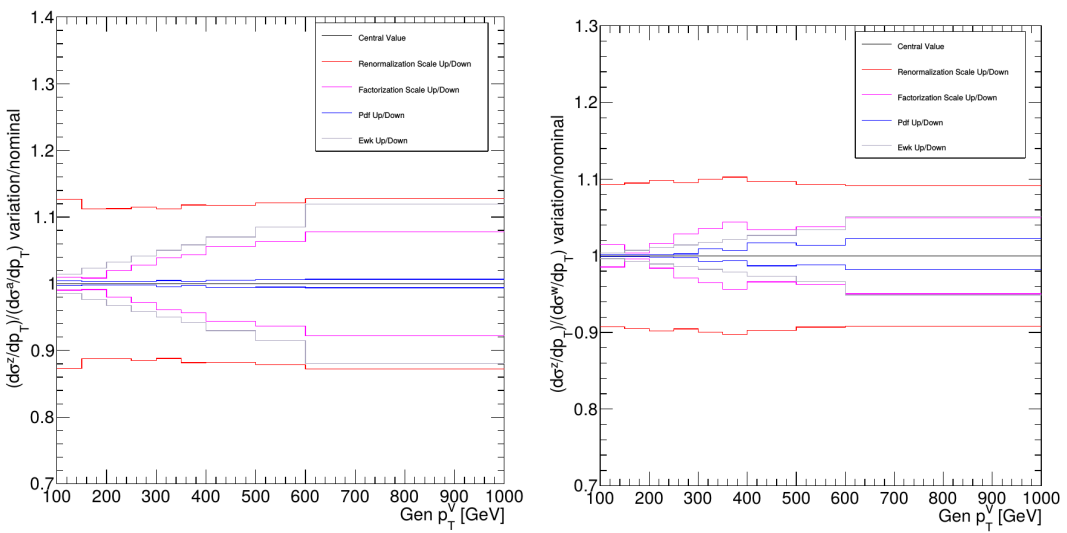


Figure 5.10: The theoretical uncertainties on the Z/γ (left) and Z/W (right) transfer factors.

1 into account the uncertainties from the jet energy scale and the jet energy resolution. The systematic un-
 2 certainties coming from variations of the factorization and renormalization scales and PDF uncertainties
 3 amount to 20% for the vector and axial signal samples and 30% for the scalar and pseudoscalar signals.

4 5.6 Results

5 The results are extracted by performing a binned fit to the missing energy spectrum, fitting simultane-
 6 ously over the five control regions and the signal region, under a given signal hypothesis. This is done
 7 using the CL_S criterion [134, 135], using the asymptotic approximation of the test statistic distributions
 8 implemented in the RooStat-based Combine tool and modelling the systematic uncertainties described in
 9 Section 5.5 as nuisance parameters. The nuisance parameter uncertainties are propagated as shape and
 10 normalization variations of the $Z(\nu\nu) + \text{jets}$ and $W(l\nu) + \text{jets}$ background. In Figure 5.11, the nuisance
 11 parameters and their uncertainties are shown before and after the fit to the data in the control regions.
 12 Before the fit they are all centred at 0 and have an uncertainty of 1. After the fit, the two largest pulls
 13 originate from the statistical uncertainty on the Z/W transfer factor and the uncertainty on the muon
 14 scale factor, but no significant tension is present in the fit and most nuisance parameters are not pulled or
 15 constrained by the fit.

16 Figures 5.12 and 5.13 show the recoil distributions in the different control regions, before and after the
 17 fit. The photon + jets control region, which has the largest yields, drives the fit and the post-fit prediction
 18 therefore corresponds well with the data. A good agreement is observed in all control regions, and the
 19 overall change in the transfer factors is relatively small.

20 Table 5.1 gives the background prediction for the various background processes in bins of missing
 21 transverse energy, using a background-only fit. Correspondingly, the fit under the background-only hy-
 22 pothesis is shown in Figure 5.14 and a good agreement is observed between the data and the prediction.
 23 The uncertainty on the recoil is below 10% for all bins.

Process	E_T^{miss} [200 – 250] GeV	E_T^{miss} [250 – 300] GeV	E_T^{miss} [300 – 350] GeV	E_T^{miss} [350 – 400] GeV	E_T^{miss} [400 – 500] GeV	E_T^{miss} [500 – 600] GeV	E_T^{miss} [> 600] GeV
$Z(\nu\nu) + \text{jets}$	19521	7473	3085	1447	1126	350	184
$W(l\nu) + \text{jets}$	15422	4793	1728	650	428	104	47.9
$Z(\ell\ell) + \text{jets}$	259	67	22.4	5.1	3.0	0.44	0.12
Top	715	240	73.8	32.5	18.3	2.9	2.5
Dibosons	148	38	8.2	2.3	0.61	0.66	0.07
QCD	773	346	157	77	64	19.5	15.8
Total	36837 ± 246	12958 ± 115	5075 ± 63	2214 ± 38	1639 ± 33	478 ± 14	250 ± 12
Observed	36858	13010	4981	2248	1614	484	260

Table 5.1: Post-fit background predictions in the signal region and observed yield. The predictions and uncertainties are obtained from the background-only simultaneous fit in the signal and control regions.

24 5.7 Improvements going from the 2015 to 2016 analysis

25 Several iterations of the monojet analysis were performed during Run 2 in 2015 and 2016, improving
 26 the achieved sensitivity with the increase in available data and additional developments to the analysis
 27 strategy, and adding new interpretations. In 2015, a first analysis with data at a centre-of-mass energy
 28 of 13 TeV was carried out [136], using data corresponding to an integrated luminosity of 2.1 fb^{-1} . In
 29 this first iteration of the search, the NLO k-factors applied to correct the LO samples used for the Z and
 30 W background estimation are derived from inclusive NLO samples, which are not binned in boson p_T .
 31 These k-factors are shown in Figure 5.15, and can be compared to the k-factors obtained from p_T -binned
 32 samples used in the following iterations of the analysis and shown in Figure 5.7.

33 In 2016, the analysis was extended to the mono-V channel [137], which can give rise to a monojet-like
 34 signature. At high p_T , the production of a W or Z boson which decays hadronically, can be effectively

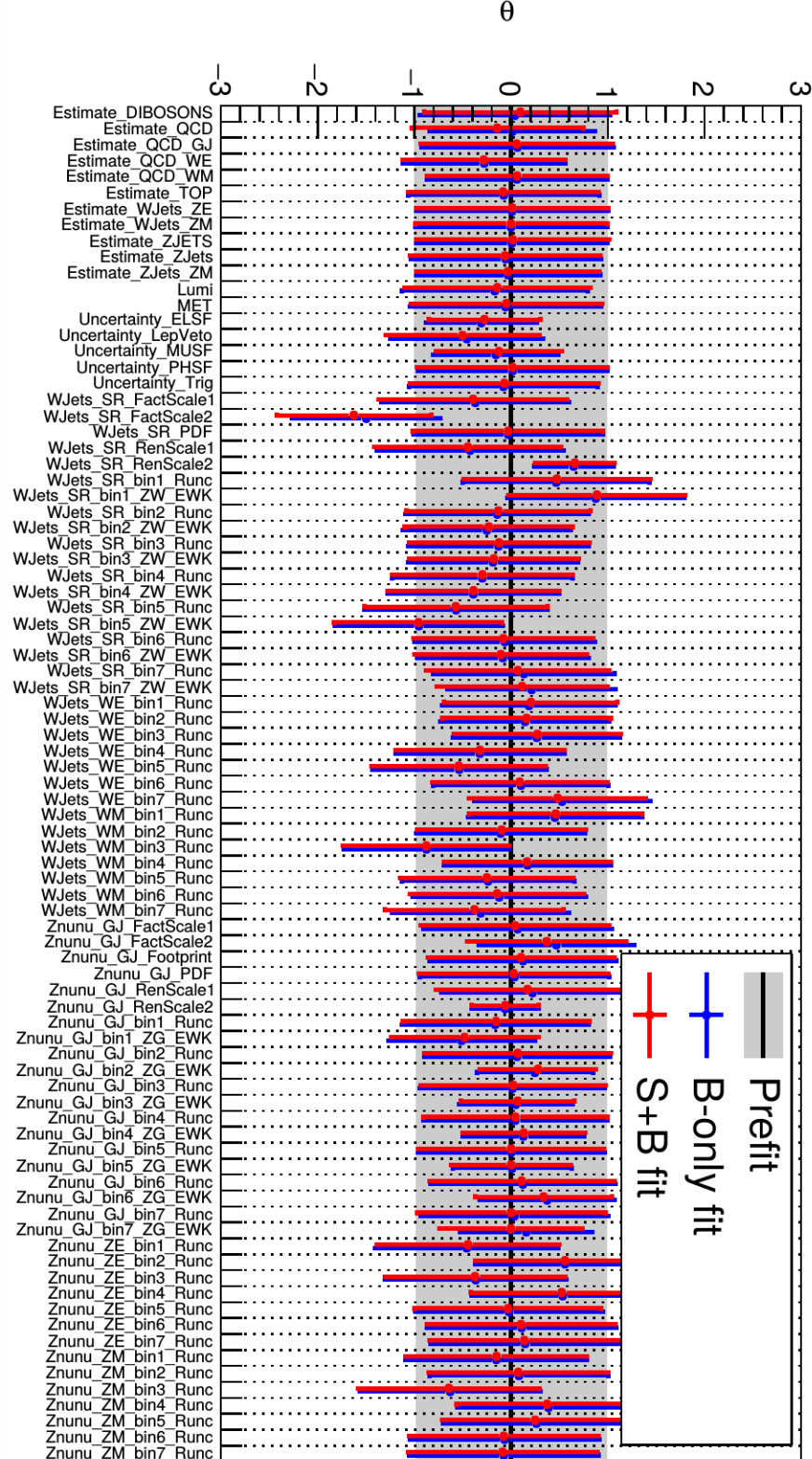


Figure 5.11: The post-fit nuisance parameters and their uncertainties, compared to the pre-fit values.

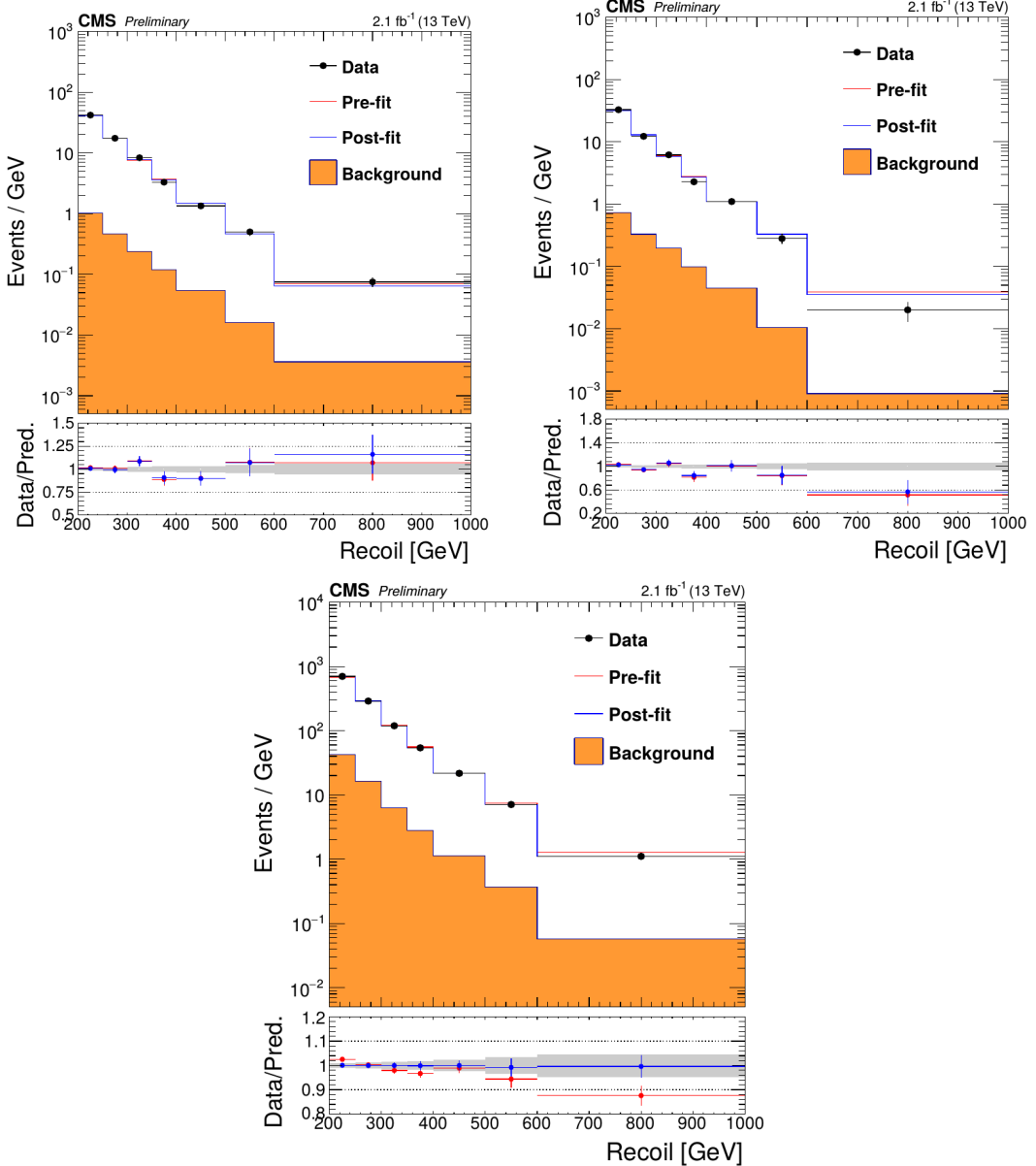


Figure 5.12: Comparison between data and prediction before (pre-fit) and after (post-fit) the simultaneous fit to the different control regions, in the dimuon (left), dielectron (right) and photon + jets (bottom) control regions. The grey band shows the uncertainty per bin, including all relevant systematic uncertainties.

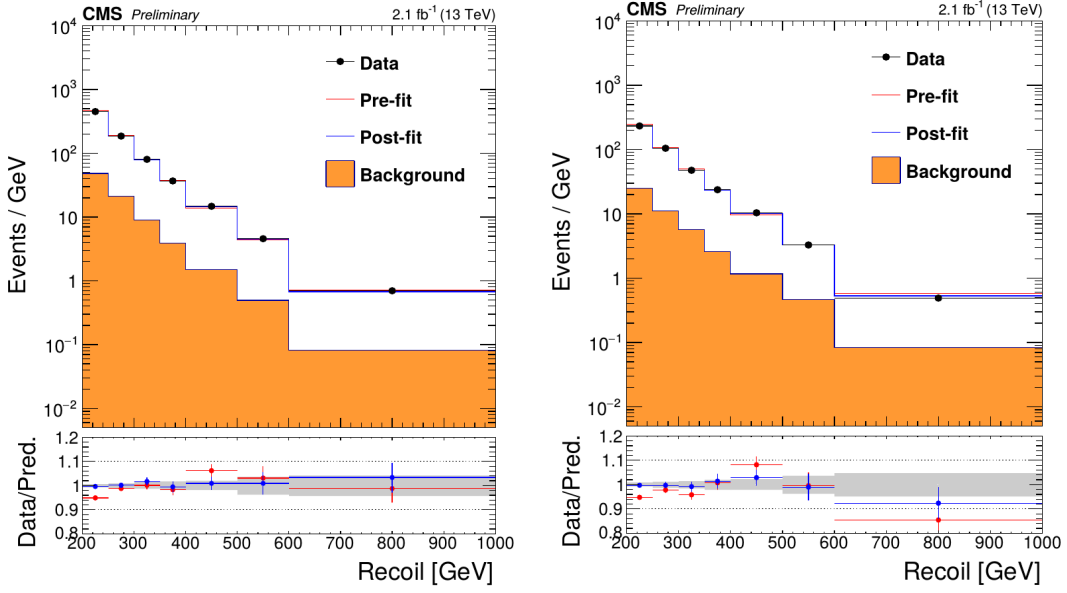


Figure 5.13: Comparison between data and prediction before (pre-fit) and after (post-fit) the simultaneous fit to the single lepton control regions, in the single muon (left) and single electron (right) control regions. The grey band shows the uncertainty per bin, including all relevant systematic uncertainties.

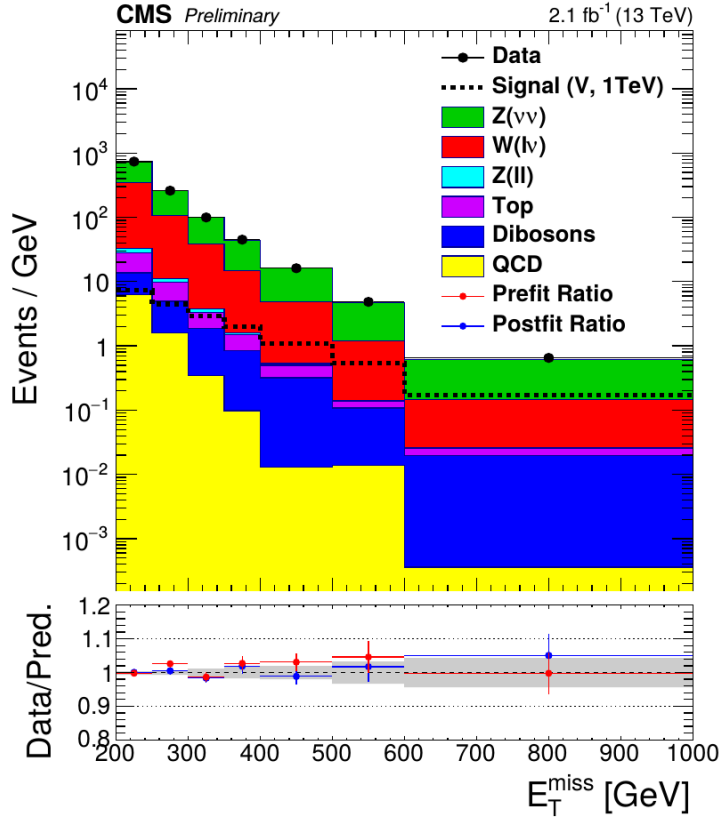


Figure 5.14: Post-fit missing transverse energy distribution for the expected backgrounds and the observed data in the signal region. The grey band indicates the post-fit uncertainty obtained from the background-only simultaneous fit in the signal and control regions.

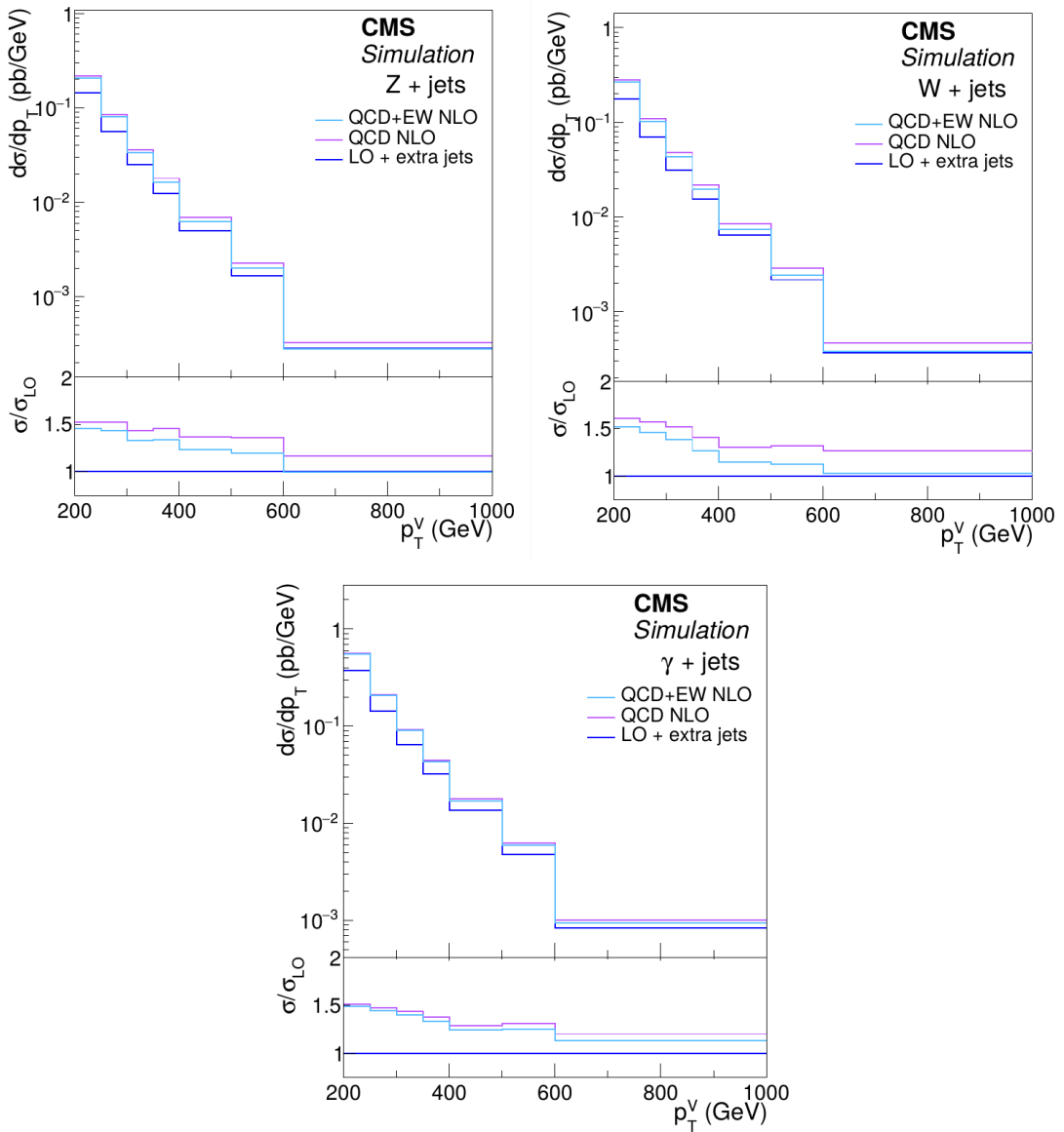


Figure 5.15: The differential cross section as a function of the boson p_T for photon, W , and Z production, using inclusive NLO samples. The resulting k-factors are shown in the ratio plots.

1 reconstructed as a single jet of large cone radius. However, in this chapter the focus is on the monojet
 2 channel and the added improvements during 2016. For this analysis, the full amount of data collected in
 3 2015 was used, corresponding to 2.3 fb^{-1} . The used NLO k-factors were derived using the p_T -binned
 4 samples, as described in Section 5.4.1.

5 A substantial difference in the next iteration of the 2016 analysis [65] is the increase in collected data,
 6 which allowed to reduce the statistical uncertainties and set stronger limits on the considered models.
 7 For these results, data collected in the first half of 2016 and corresponding to an integrated luminosity
 8 of 12.9 fb^{-1} were available. One of the improvements that were added is the direct use of MC samples
 9 generated at leading order for the estimation of the main backgrounds. This was possible by generating
 10 samples that are binned in W boson p_T . As a result, no k-factors need to be applied to the $W + \text{jets}$
 11 sample and no additional systematic uncertainties are to be introduced for this. Figures 5.16 and 5.17
 12 show the obtained reduction in the overall post-fit uncertainty on the predictions in the 5 control regions.

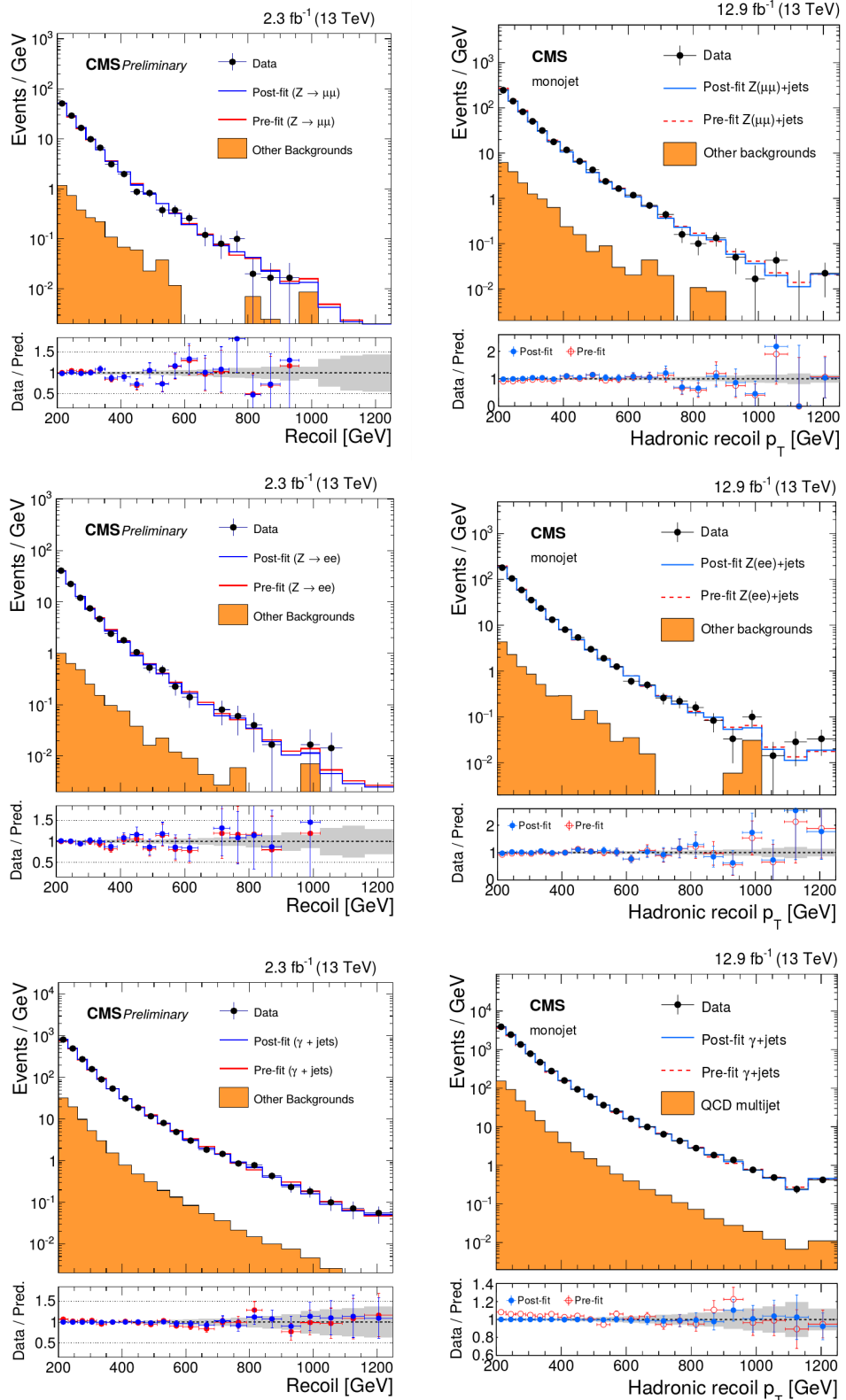


Figure 5.16: Comparison of the hadronic recoil p_T distribution between the data and MC simulation in the dimuon (top), dielectron (middle), and photon + jets (bottom) control regions, showing the reduction in overall post-fit uncertainty (grey band) going from the early 2016 analysis (left) to the analysis using data from the first half of 2016 (right). The fit was performed simultaneously over all the control and signal regions, assuming the absence of any signal. The last bin includes all events with hadronic recoil $pT > 1160$ GeV. Figures taken from [137] and [65].

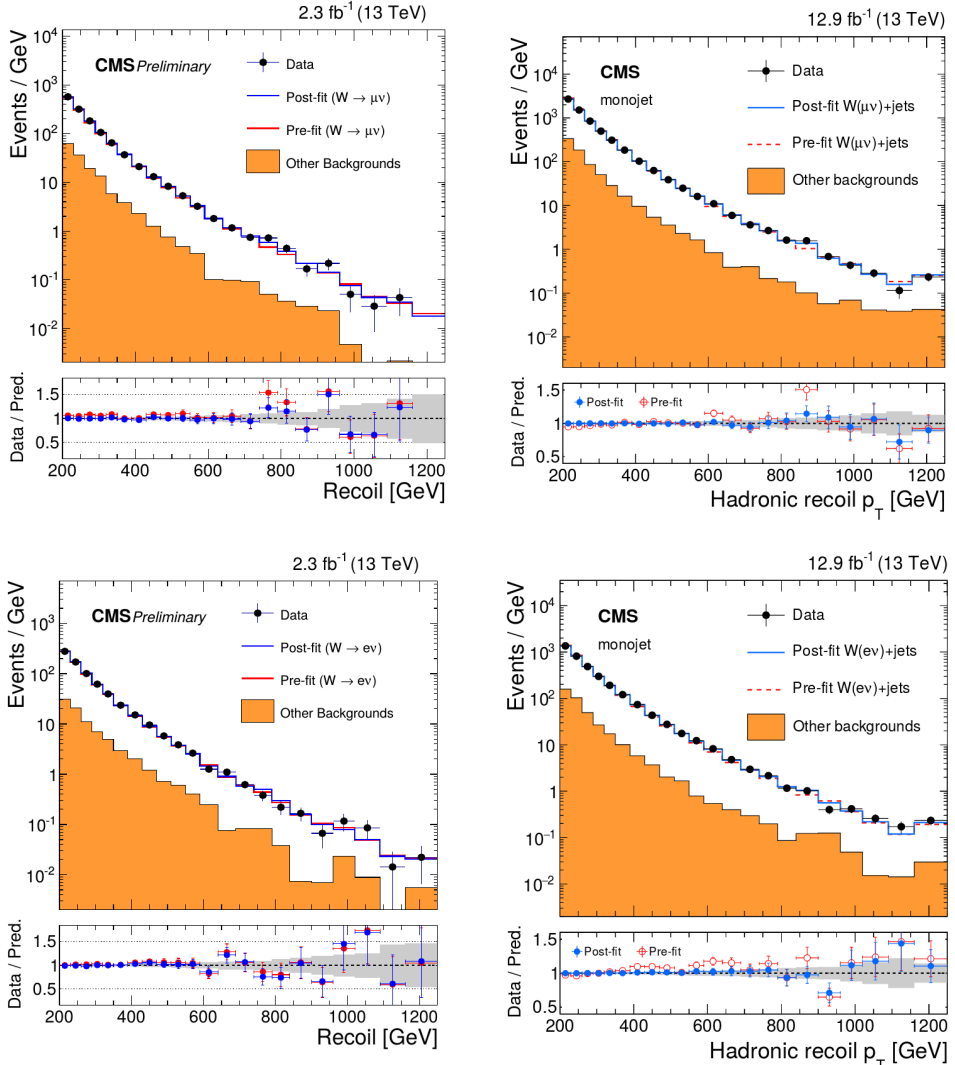


Figure 5.17: Comparison of the hadronic recoil p_T distribution between the data and MC simulation in the single muon (top) and single electron (bottom) control regions, showing the reduction in overall post-fit uncertainty (grey band) going from the early 2016 analysis (left) to the analysis using data from the first half of 2016 (right). The fit was performed simultaneously over all the control and signal regions, assuming the absence of any signal. The last bin includes all events with hadronic recoil $pT > 1160$ GeV. Figures taken from [137] and [65].

5.8 Interpretation

- The results of the second iteration of this search, using the mono-V final state as well, are interpreted in terms of simplified dark matter models assuming a vector, axial-vector, scalar, or pseudoscalar mediator decaying to a pair of fermionic dark matter particles, as described in Section 2.2.4. As no significant excess was observed, upper limits are placed 95% confidence level (CL) on the ratio of the signal cross section to the predicted cross section, $\mu = \sigma/\sigma_{th}$. These limits are shown as a function of the mediator mass (m_{med}) and the dark matter mass (m_{DM}) in Figures 5.18 and 5.19, for the four types of mediators. The regions where the 95% CL upper limits on μ are less than one are considered to be excluded.

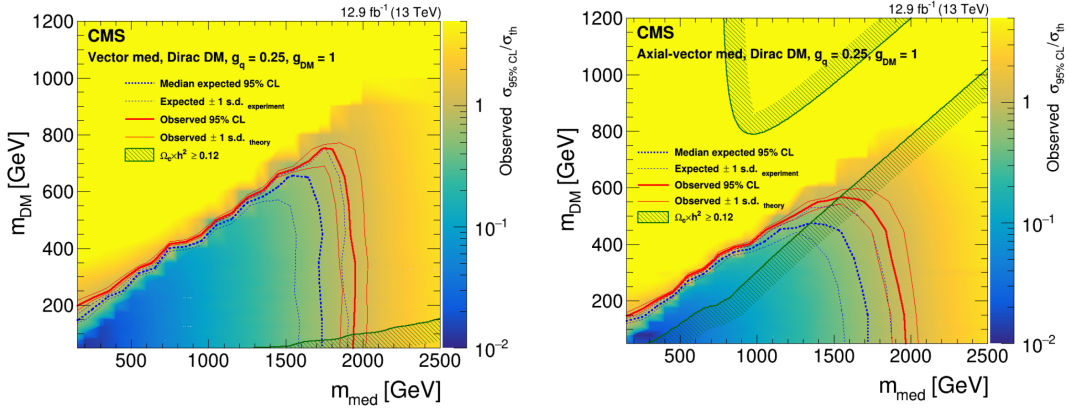


Figure 5.18: The 95% CL upper limits on the $\mu = \sigma/\sigma_{th}$ in the $m_{\text{med}} - m_{\text{DM}}$ plane, for a vector (left) or axial-vector (right) mediator. The cosmological constraints from the WMAP and Planck measurements of the CMB are shown as well. Figures taken from [65].

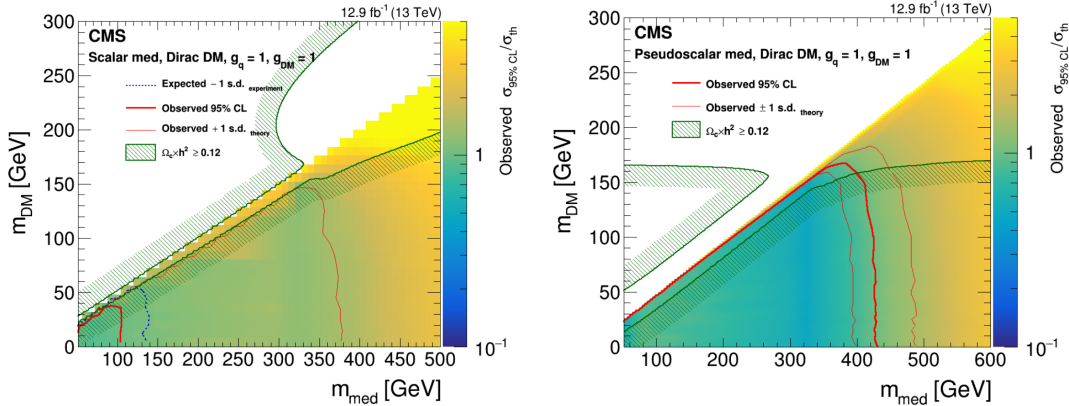


Figure 5.19: The 95% CL upper limits on the $\mu = \sigma/\sigma_{th}$ in the $m_{\text{med}} - m_{\text{DM}}$ plane, for a scalar (left) or pseudoscalar (right) mediator. The cosmological constraints from the WMAP and Planck measurements of the CMB are shown as well. Figures taken from [65].

- For the vector and axial-vector models, mediator masses up to 1.95 TeV are excluded, while mediator masses up to 100 GeV and 430 GeV can be excluded for the scalar and pseudoscalar models, respectively. Figures 5.18 and 5.19 also show the constraint from the observed cosmological relic density of dark matter, which was determined from the WMAP and Planck CMB measurements. The expected dark matter abundance is estimated using a thermal freeze-out mechanism and compared to the observed cold dark matter density, assuming that the considered dark matter candidate is the dominant component of the observed dark matter.

The obtained limits can also be translated into 90% CL upper limits on the dark matter-nucleon scattering cross section $\sigma_{\text{SI/SD}}$, in order to compare them to results from direct detection experiments.

- 1 The exclusion contours in the $m_{\text{DM}} - \sigma_{\text{SI/SD}}$ plane are obtained following the approaches outlined in
 2 [138–140], where σ_{SI} stands for spin-independent and σ_{SD} for spin-dependent dark matter-nucleon cross
 3 section. The resulting limits are show in Figures 5.20 and 5.21.

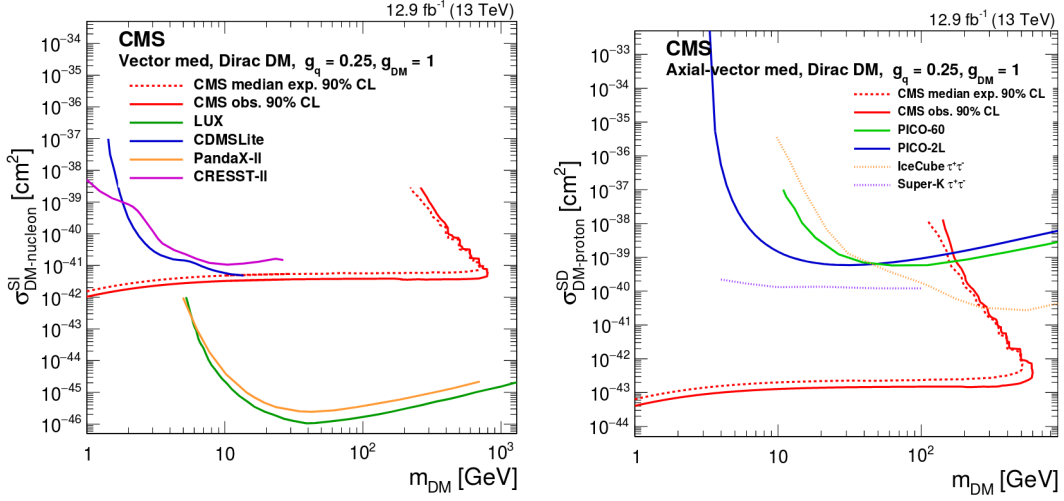


Figure 5.20: The 90% CL upper limits in the $m_{\text{DM}} - \sigma_{\text{SI/SD}}$ plane, for a vector (left) or axial-vector (right) mediator. Figures taken from [65].

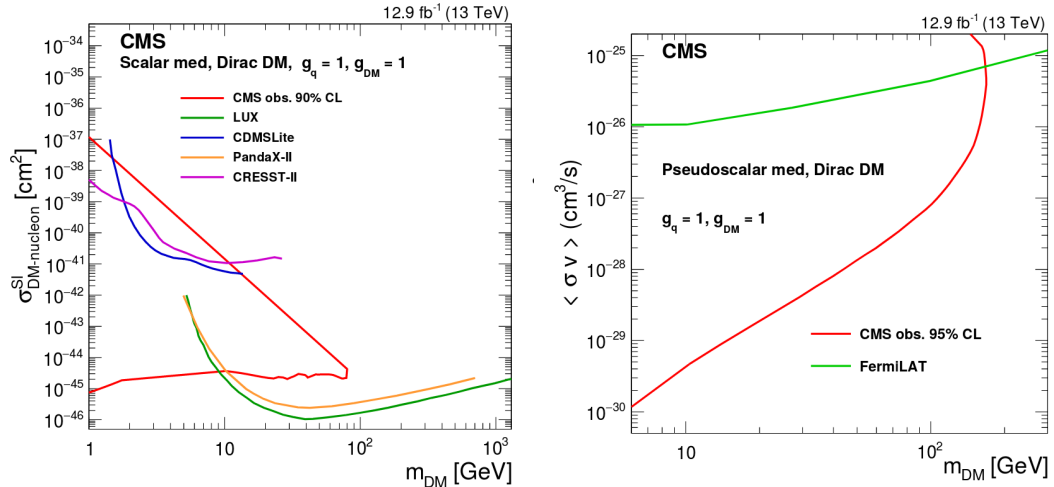


Figure 5.21: The 90% CL upper limits in the $m_{\text{DM}} - \sigma_{\text{SI/SD}}$ plane, for a scalar (left) or pseudoscalar (right) mediator. Figures taken from [65].

- 4 For the vector and scalar mediators, the 90% CL upper limits on the spin-independent cross section
 5 are compared to results from the CDMSLite [141], LUX [142], PandaX-II [143], and CRESST-II [144]
 6 experiments. This shows that monojet limits are complementary to the results from the direct detection
 7 experiments at low dark matter masses. The 90% CL upper limits on the spin-dependent cross section ob-
 8 tained for the axial-vector mediator are compared to the PICO-2L [145], PICO-60 [146], IceCube [147],
 9 and Super Kamiokande experiments [148]. In the case of the pseudoscalar mediator, the limits are com-
 10 pared to the indirect detection results from the Fermi-LAT experiment [149, 150]. In the considered
 11 scenario the dark matter annihilates into b quark pairs in the centre of the galaxy, producing gamma rays.